

Research Article

Ring Expansion with a Stepped Conical Punch to Extract the Workability Diagram in Bulk Metal Forming for C22000 Alloy: Experiments and Numerical Simulation with Ductile Damage Model

S.M. Seyyed Hatami, H. Lexian and M. Khandaei*

Faculty of Material and Manufacturing Technologies, Malek Ashtar University of Technology, Iran

ARTICLE INFO

Article history:

Received 28 December 2024

Reviewed 24 March 2025

Revised 2 June 2025

Accepted 7 July 2025

Keywords:

Workability

C22000

Ring expansion test

Anisotropic ductile damage

Bulk metal forming

Please cite this article as:

Seyyed Hatami, S. M., Lexian, H., & Khandaei, M. (2025). Ring expansion with a stepped conical punch to extract the workability diagram in bulk metal forming for C22000 alloy: Experiments and numerical simulation with ductile damage model. *Iranian Journal of Materials Forming*, 12(3), 20-32.
<https://doi.org/10.22099/IJMF.2025.52038.1314>

ABSTRACT

Workability is a measure of the extent of deformation that a material can withstand before failure in bulk forming processes. In these processes, ductile fracture is the most common failure mode. In this study, ring expansion tests with a stepped conical punch were performed on samples with different geometries. For each strain path, axial and circumferential strains were calculated, and the right side of workability diagram was extracted. The primary objective of this paper is to determine the workability of C22000 alloy by fracture in mode I of fracture mechanics, which involves crack opening by tension. This study is the first, to the authors' knowledge, to simultaneously determine the right side of the workability diagram using anisotropic ductile damage mechanics. The formulation was developed within the framework of thermodynamics of irreversible processes, and a symmetric second-order tensor was used to describe the anisotropic damage state variable. The model was implemented using VUMAT coding and ABAQUS/Explicit software to simulate experimental tests. In order to display the workability diagram numerically, the adopted approach is based on the determination of damage values. Previous strain measurements were made just before crack initiation, and thus, with this method, the extraction of the diagram is done more comprehensively. The results show that different levels of damage and damage evolution can represent distinct regions of the workability diagram.

© Shiraz University, Shiraz, Iran, 2025

1. Introduction

Workability refers to the relative ease with which a metal can be shaped through plastic deformation. The term workability is often used interchangeably with formability, which is preferred when referring to sheet

metal forming. However, workability is generally used to describe the forming of materials through bulk metal forming processes. In bulk metal forming, workability is limited by issues such as buckling, folding of material over itself, formation of laps, or fracture.

* Corresponding author

E-mail address: m_khandaei@mut.ac.ir (M. Khandaei)

<https://doi.org/10.22099/IJMF.2025.52038.1314>

Before failure occurs in bulk forming processes, ductile fracture is the most common mode of failure. It is a complicated phenomenon that depends on process parameters such as stress, strain, strain rate, friction and forming temperature, as well as material parameters such as strain hardening and the volume fraction of voids and second-phase particles [1]. Due to this complexity, various criteria have been proposed to evaluate workability. The empirical criteria are either stress-based or strain-based. Common theoretical criteria are based on the growth and coalescence of voids.

The techniques of continuum damage mechanics have been used to predict ductile fracture. Tie-Jun [2] formulated a local criterion for ductile fracture. Another criterion, similar to the continuum damage mechanics technique, was formulated by Lemaitre in 1985 [3].

Workability does not always correlate with ductility measured in a tension test, especially if cracking starts on the surface. For this reason, other tests are often used.

Kuhn (1978) [4] proposed a simple procedure for evaluating workability using upset compression tests. The barreling phenomenon during upsetting causes circumferential tensile stresses that may lead to cracking. He plotted the circumferential strain (ϵ_θ) when the first cracks were observed as a function of the axial strain (ϵ_z). The ratio of strains was varied by changing the lubrication and the height-to-diameter ratio of the specimens. In Fig. 1, a schematic of the left side of the workability diagram for bulk metal forming processes is selected from the ASM Handbook. The fracture line is drawn for two different types of materials using the compression test method. The path of strain (a and b) for two types of bulk forming process is presented for comparison with the workability diagram. Strain path (a) would lead to failure for material A, while both strain paths (a and b) can be used for the successful forming of material B [5].

Failure by surface or internal cracking in bulk metal forming is caused by the accumulation of ductile damage within regions that are highly strained due to extensive plastic flow. Apart from special purpose processes such as the shearing of bars and bar sections, where cracks are needed to cut material, the occurrence of cracks is generally

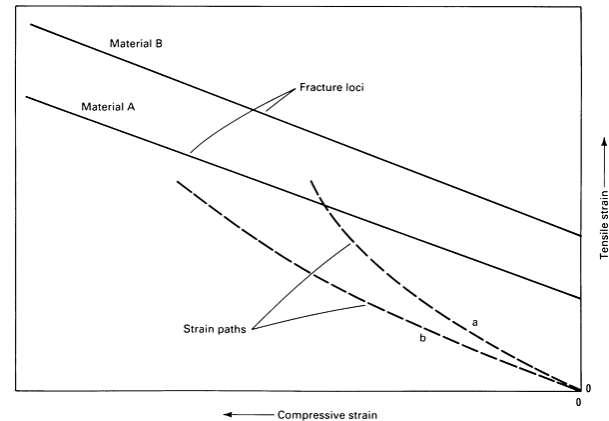


Fig. 1. Schematic of the left side of the workability diagrams for bulk forming processes [5].

undesirable and should be prevented during process design.

Currently-available finite element computer programs may aid this objective, but appropriate input data regarding a relevant fracture locus is crucial for successfully predicting the onset of cracking in bulk metal forming.

The damage mechanics method can be used to predict the behavior of materials in forming processes. Damage mechanics deals with the effects of the initiation, coalescence and growth of micro voids leading to the final failure of materials. Among the models introduced in the literature, the Saanouni anisotropic damage model has the advantage of being used extensively, not only by the provider of the model but also by other researchers, and is considered a powerful model in metal forming processes.

Salehi Nasab et al. [6] carried out the numerical implementation of an advanced elastic-plastic model fully coupled with anisotropic ductile damage. The implemented formulation has been defined within the framework of the thermodynamics of irreversible processes, and a symmetric second-order tensor was adopted to describe the anisotropic damage state variable. This model is fully coupled with nonlinear isotropic hardening and nonlinear kinematic hardening, and is used to simulate metal forming processes. Yetna N'Jock et al. [7] coupled the distortional hardening model with the Saanouni ductile damage model. The effect of distortional parameters and isotropic ductile damage on spring back has been investigated. Nakazima tests [8] (2014) and Marciniak tests [9] (2015) have been

used for the experimental extraction of FLD diagrams, and the Saanouni damage model has been used for their validation.

In addition to the recent references, the Saanouni damage model has been evaluated by researchers in other works and validated with different alloys and processes. Saanouni has evaluated the classical side-pressing of a cylinder with infinite length (plane strain case) on aluminum alloy, as well as the cold extrusion of a cylindrical bar on steel [10]. Saanouni et al. [11] investigated the processes of hot forging and cold extrusion on steel. Rajhi et al. [12] validated the upsetting of a cylindrical billet process with stainless steel grade AISI 316L using the Saanouni damage model.

Therefore, the high ability to consider the effects of damage anisotropy, the simplicity of the model, the tests required to determine the material constants, the use of the hypothesis of total energy equivalence, and the successful results in predicting the bulk metal forming processes are among the most important reasons for the selection of the Saanouni model in this study. Thermodynamically consistent, non-associative, and fully anisotropic elastoplastic constitutive equations, strongly coupled with ductile anisotropic damage, were developed in the Saanouni anisotropic damage model used in this study, which included Hill's yield criterion and combined nonlinear isotropic and kinematic hardening. The implemented formulation was defined in the framework of thermodynamics of irreversible processes, and a symmetric second-order tensor was adopted to describe the anisotropic damage state variable. In previous studies, the Saanouni damage model has not been used to extract the workability diagram, and the behavior of the C22000 alloy has not been challenged with the Saanouni damage model.

This paper revisits workability in light of fundamental concepts of plasticity and anisotropic ductile damage. It uses a test to appraise the accuracy, reliability and validity of fracture loci associated with crack opening under loading conditions different from those found in conventional tests for workability. Hosford (2011) [13] presented a simple test to measure

the circumferential fracture strain when a hollowed tube of the work material is expanded by pushing it onto a conical tool. In this study, the test presented by Silva et al. [14] has been used. The workability test consists of expanding rings of various wall thicknesses with a stepped conical punch, allowing for the investigating of fracture initiation under three-dimensional states of stress subjected to various magnitudes of stress triaxiality.

To display the workability numerically, the adopted approach is based on determining damage values. Previous experimental measurements of axial and circumferential strains were done just before crack initiation, but the damage level was unknown. With this method, the extraction of the diagram has been done more comprehensively. The Saanouni anisotropic ductile damage model has been used to extract the strain loading paths and plot the corresponding workability of C22000 by the fracture line. Different levels of damage and damage evolution can be used to express different regions of the workability diagram.

2. Experimental Procedure

Copper alloy (C22000) was prepared from the local market in the form of a sheet with dimensions of $2000 \times 600 \times 10$ mm, and the samples for conducting tests to identify the behavior of the alloy were separated from the same sheet, according to the test conditions. The chemical analysis of this alloy, based on the weight percentage of elements, was conducted. A ring compression test was performed to determine the friction factor m on an alloy cylinder. The ring compression test was plotted against the deformation on Male and Cockcroft [15] calibration curves. It was found that the friction factor m was equal to 0.30.

The workability tests were designated as ring expansion with a stepped conical punch. These tests were performed to extract the right side of the workability diagram in bulk forming on C22000 alloy. The tests were performed at room temperature using a hydraulic press machine with a speed of 5 mm/min. The expansion of the ring with the conical punch led to the creation of a crack at the inner conical edge, covering the

strain paths on the right side of the workability diagram. The punch was made of cold working tool steel, hardened and tempered to a Rockwell hardness of HRC 60. The specimens were machined from the supplied C22000 alloy according to geometry provided in Table 1. The exact moment of cracking was obtained using an experimental test. This test was based on a phenomenon characterized by crack initiation with a drop in force. The procedure to determine the strain loading paths up to fracture in ring expansion with a stepped conical punch was performed by inverse identification of strains at location 'S' of Table 1 using finite element analysis. This was necessary because it is difficult to engrave rectangular grids on the inner ring surfaces, and they vanish during expansion with the stepped conical punch. Therefore, it was not possible to determine the strain loading paths to fracture in ring expansion with a stepped conical punch by experimental testing at location 'S'.

According to Eq. (1), axial and circumferential strain (ε_z , ε_θ) values were calculated from these measurements.

$$\varepsilon_z = \ln\left(\frac{t}{t_0}\right), \varepsilon_\theta = \ln\left(\frac{w}{w_0}\right) \quad (1)$$

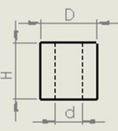

Different strain paths were drawn on the axial strain and circumferential strain diagram, and their endpoints were selected as fracture points. All endpoints were fitted and interpolated. The interpolated line represents the fracture lines in the workability diagram.


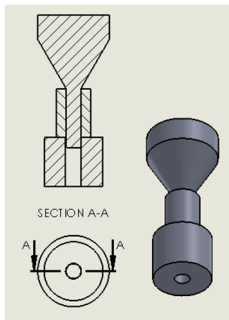

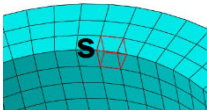



3. Ductile Damage Model

The Saanouni anisotropic damage model, due to its special assumptions and theory, has been of great interest in the numerical analysis of the forming processes of metallic materials. The ductile damage anisotropy is described by a symmetric second-rank tensor, and its effect on the mechanical fields is described by a symmetric fourth-rank tensor. This model is developed within the framework of non-associative plasticity theory. The quadratic Hill'48 yield criterion and non-linear (isotropic/kinematic) hardening are considered in the associated flow rule model. The numerical formulation of the proposed model is implemented in ABAQUS finite element code via the user material subroutines VUMAT.

Using a thermodynamically-consistent framework, the effective state variables are defined to introduce the

Table 1. Geometry of ring expansion tests to determine the right side of the workability diagram

Geometry				
	D(mm)	H(mm)	d(mm)	
				
				

1	Expansion_4	4	10	3				
2	Expansion_5	5	10	3				
3	Expansion_6	6	10	3				
4	Expansion_7	7	10	3				

effect of the anisotropic damage through the total energy equivalence assumption. Based on the total energy equivalence hypothesis, it is assumed that the total energy for an RVE in its real deformed and damaged configuration is equal to the total energy of an RVE in a virtual and undamaged configuration [16]. If the total energy is assumed to be the sum of three parts namely: The elastic energy, the energy stored in kinematic hardening and the energy stored in isotropic hardening, then the energy equivalence principle is applied separately to each energy component [17].

Different definitions for the damage-effect operator have been considered in previous research. The damage effect-tensor deduced from the Murakami and Ohno symmetrization [18] is chosen in this study, as given in Eq. (2):

$$M_{ij}(d) = \begin{pmatrix} \frac{1}{1-d_1} & 0 & 0 & 0 & 0 & 0 \\ 0 & \frac{1}{1-d_2} & 0 & 0 & 0 & 0 \\ 0 & 0 & \frac{1}{1-d_3} & 0 & 0 & 0 \\ 0 & 0 & 0 & \frac{2-d_1-d_2}{2(1-d_1)(1-d_2)} & 0 & 0 \\ 0 & 0 & 0 & 0 & \frac{2-d_2-d_3}{2(1-d_2)(1-d_3)} & 0 \\ 0 & 0 & 0 & 0 & 0 & \frac{2-d_1-d_3}{2(1-d_1)(1-d_3)} \end{pmatrix} \quad (2)$$

All these aspects are extensively presented in many previous publications and a comprehensive summary can be found in Badreddine (2015) [17]. It was calibrated at a constant temperature.

3.1. Material model identification

Identifying the material constants of the elastoplasticity model coupled with anisotropic damage is necessary for the implementation of the Saanouni damage model in numerical simulation. Elastoplasticity parameters and damage coefficients are presented in Table 2.

In the first step, the elastoplasticity parameters of the material Hill (F, G, H, L, M, N), σ_y , ν , E , and G , were identified with the help of experimental tests up to a certain strain without considering the effect of damage.

There are different methods to measure the elastic modulus. The Ultrasonic sound velocity measurement (USVM) technique was used in this study [19]. The velocity of longitudinal and transverse ultrasonic waves in three cylindrical samples was measured in three directions of rolling, transverse to rolling and in the

direction of thickness. The value was calculated. The values of C_t , represent the transverse wave speed in (m/s) unit, C_l , represents the longitudinal wave speed in (m/s), and ρ , is the density of the material. The equations of Young's modulus, shear modulus, Poisson's ratio and test results are reported in Table 3.

The uniaxial tensile test was performed according to the ASTM standard, E8/E8M-13a. After the curve fitting, the true stress-strain diagram of the uniaxial tension test was extracted. The yield stress value was determined to be 224 MPa.

Table 2. Elastoplasticity parameters and damage coefficients

E	Young modulus	(GPa)
G	Shear modulus	(GPa)
F, G, H, L, M, N	Hill plastic anisotropy coefficients	-
Q	The isotropic hardening modulus	(MPa)
b	The isotropic hardening saturation parameter	-
C	The kinematic hardening modulus	(MPa)
a	The kinematic hardening saturation parameter	-
S	The damage evolution parameter	$\left(\frac{J}{\text{mm}^3}\right)$
s	The damage evolution parameter	-
β	The damage evolution parameter	-
γ	Material constant	-
Y_0	Damage energy release rate threshold	$\left(\frac{J}{\text{mm}^3}\right)$

To extract Hill plastic anisotropy coefficients (F, G, H, L, M, N), the method of extracting anisotropy coefficients is different for their use in the bulk forming process. Compression tests are used to extract these coefficients. Kitamura et al. [20] presented a method for the small-cube compression test. These tests are used for thick metal plates and exhibits plastic anisotropy properties in the thickness direction. Small cubes for compression tests were cut from alloy sheet C22000 with a thickness of 10 mm using the electrical discharge machining (EDM) process in the directions shown in Fig. 2 and were prepared with dimensions of $7 \times 7 \times 7$ mm. The compression test was done on small cubes with a pressure ratio of 50% and the square shape in the cubes becomes rectangular due to the anisotropy of the plastic.

Table 3. Ultrasonic test results

Direction	C_l (m/s)	C_t (m/s)	ρ (kg/m ³)	Elastic modulus (E) (GPa)	Shear modulus (G) (GPa)	ν
Directions of rolling	4220.5	2171	8800	110	41.5	0.32
Transverse to rolling	4521.2	2171	8800	112	41.5	0.35
Direction of thickness	4562.8	2171	8800	112	41.5	0.35

$$E = \frac{\rho C_t^2 \left[3 \left(\frac{C_l}{C_t} \right)^2 - 4 \right]}{\left(\frac{C_l}{C_t} \right)^2 - 1}$$

$$G = \rho C_t^2 \quad \nu = \frac{\left(\left(\frac{C_l}{C_t} \right)^2 - C_t^2 \right)}{C_l^2 - C_t^2}$$

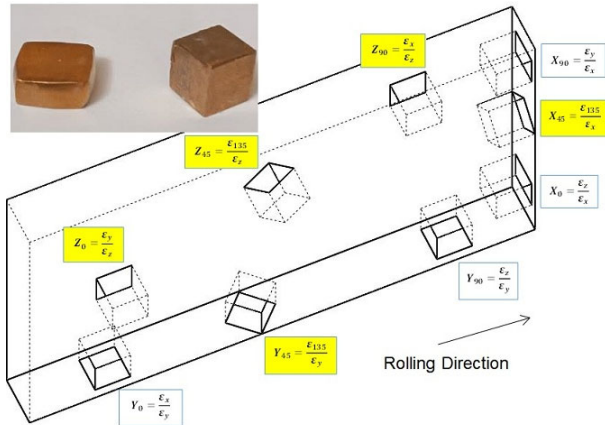


Fig. 2. Extraction of 5 small cubes from a thick alloy sheet to extract anisotropy coefficients.

Finally, Hill anisotropy coefficients for C22000 alloy were extracted. The values of the Hill anisotropy coefficients are $F = 1.01$, $G = 0.98$, $H = 0.77$, $L = 3.28$, $M = 3.66$ and $N = 2.55$.

In the second step, the damage tensor components were calculated according to the structural equations of the Saanouni damage model and the relationship between the modulus of elasticity of the material in undamaged state and damaged state. The main components of the anisotropic damage tensor were defined according to Eq. (3):

$$d_i = 1 - \sqrt{\frac{\tilde{E}_i}{E}} \quad (3)$$

Ultrasonic method was used to determine the changes of elasticity modulus in three directions of rolling, perpendicular to rolling and also in the direction of thickness. The damage tensor components were determined in three directions. The working method involved extracting a sample from the C22000 alloy sheet by machining to perform the uniaxial tensile test. After performing the tensile test in the positions shown in Fig. 3, the rectangular cube pieces were extracted and

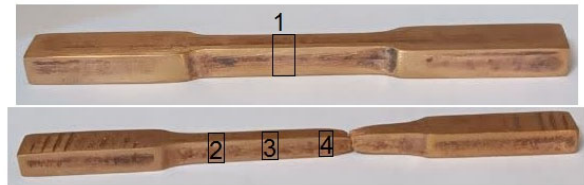
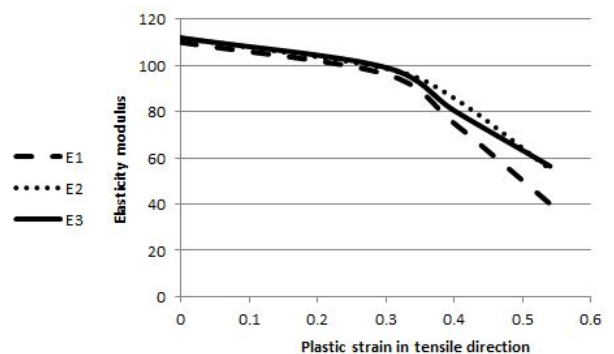


Fig. 3. Uniaxial tensile test sample to determine damage tensor components in 4 different positions.

the new elastic modulus \tilde{E} was measured in three directions using the ultrasonic method.

The total reduction in width and thickness of the sample was a suitable measure for the plastic strain in the direction of tensile, $\varepsilon_l = -(\varepsilon_w + \varepsilon_t)$. Using $E1$, $E2$ and $E3$ curves were drawn with respect to plastic strain as shown in Fig. 4. The non-compliance of $E1$, $E2$ and $E3$ curves indicates the nature of damage anisotropy. In fact, Young's modulus grows faster in one direction (rolling direction) than in the other two directions. The amount of critical damage was determined using Eq. (3) calculated in the direction of rolling as 0.396, perpendicular to the direction of rolling as 0.298, and in the direction of thickness as 0.290.

In the last step, the damage growth parameters as well as the hardening coefficients were determined according to the results of Saanouni's research paper. Saanouni et al. [21], due to the difficulty of extracting

Fig. 4. Experimental growth of damaged elastic modulus $E1$, $E2$ and $E3$ with respect to plastic strain.

coefficients by numerical and experimental combined methods, as well as the lack of access to optical measuring devices and the high cost of their services, used a wide range of virtual materials and suggested them as a suitable alternative for selecting material parameters. In subsequent studies, researchers have used its results for material parameters and acceptable comparative results have been presented. A wide range of "virtual" materials have presented by choosing appropriate values of material parameters as follows: ($A0$, $A1$, $A2$, $B0$, $B1$ and $B2$). Virtual materials are divided into two main groups, $A0$ and $B0$, representing a material class characterized by a "short" hardening stage or "large" hardening stage. These "virtual" materials cover a wide class of real metallic materials, ranging from aluminum alloys to high-strength steels. The presented parameters can be used in the simulation of metal forming processes. According to the above grouping, C22000 alloy was placed in $A2$ group and coefficients with values of $C = 10$ GPa, $Q = 1000$ MPa, $a = 100$, $b = 50$, $s = \beta = 1$, and $S = 2.8$ MPa were considered for the alloy. Also, coefficients $\gamma = 1$ and $Y_0 = 0$ were considered for the alloy [16].

4. Numerical Aspects

The implemented formulation has been defined in the framework of thermodynamics of irreversible processes and a symmetric second-order tensor was adopted to describe the anisotropic damage state variable. The damage model was implemented with VUMAT coding and ABAQUS/Explicit software.

The global equilibrium problem was solved using the displacement-based finite element method. This requires the numerical integration of the fully coupled anisotropic constitutive equations at each Gauss point of each finite element. All these aspects are presented in the reference of Saanouni Handbook 2012 [16].

In this section, and for the sake of brevity, the focus is on the local integration of the anisotropic constitutive equations. This involves the computation of the overall mechanical unknowns (σ_{n+1} , X_{n+1} , R_{n+1} , d_{n+1}) at the end of the time interval t_{n+1} knowing their values (σ_n , X_n , R_n , d_n) at the beginning of the same time interval t_n .

The constitutive equations were defined a set of nonlinear ordinary differential equations (ODEs) to be numerically integrated at each quadrature point of each finite element. The plastic and damage flow relationships were numerically integrated using a fully implicit and iterative integration scheme, while the asymptotic integration scheme was applied to both kinematic and isotropic hardening evolution relationships. As a result, the number of equations was reduced to five equations.

The constitutive equations were rewritten as Eqs. (4) to (8) after integration.

$$f_{n+1}^p = \|\tilde{\sigma}_{n+1} - \tilde{X}_{n+1}\|_H = -\frac{R_{n+1}}{\sqrt{1 - \|d_{n+1}\|}} - \sigma_y = 0 \quad (4)$$

$$g_{n+1}^p = \varepsilon_{n+1}^p - \varepsilon_n^p - \Delta\lambda n_{n+1} = 0 \quad (5)$$

$$g_{n+1}^d = d_{n+1} - d_n - \frac{\Delta\lambda}{(1 - \|d_{n+1}\|)^\beta} \frac{\|Y_{n+1}\| - Y_0^s}{S} n_{n+1} = 0 \quad (6)$$

$$g_{n+1}^\alpha = \alpha_{n+1} - \alpha_n e^{-a\Delta\lambda^p} - \frac{(1 - e^{-a\Delta\lambda^p})}{a} n_{n+1} = 0 \quad (7)$$

$$g_{n+1}^r = r_{n+1} - r_n e^{-b\Delta\lambda^p} - \frac{(1 - e^{-b\Delta\lambda^p})}{b\sqrt{1 - \|d_{n+1}\|}} = 0 \quad (8)$$

The set of equations (Eqs. (4) to (8)) leads to a nonlinear system that can be solved according to the elastic prediction-plastic correction algorithm.

1- Elastic predictor:

The trial stress was calculated using Eq. (9):

$$\sigma_{n+1}^{trial} = \sigma_n + \tilde{C}_n : \Delta\varepsilon \quad (9)$$

In Eq. (9), \tilde{C}_e is the anisotropic elasticity operator. It was defined according to Eq. (10) and \tilde{C}_n was defined according to Eq. (11):

$$C_e = \begin{pmatrix} \frac{E_1(1 - \nu_{32}\nu_{23})}{\Delta} & \frac{E_2(\nu_{12} + \nu_{13}\nu_{32})}{\Delta} & \frac{E_3(\nu_{13} + \nu_{12}\nu_{23})}{\Delta} & 0 & 0 & 0 \\ \frac{E_1(\nu_{21} + \nu_{23}\nu_{31})}{\Delta} & \frac{E_2(1 - \nu_{13}\nu_{31})}{\Delta} & \frac{E_3(\nu_{23} + \nu_{21}\nu_{13})}{\Delta} & 0 & 0 & 0 \\ \frac{E_1(\nu_{31} + \nu_{32}\nu_{23})}{\Delta} & \frac{E_2(\nu_{32} + \nu_{12}\nu_{31})}{\Delta} & \frac{E_3(1 - \nu_{21}\nu_{12})}{\Delta} & 0 & 0 & 0 \\ 0 & 0 & 0 & G_{12} & 0 & 0 \\ 0 & 0 & 0 & 0 & G_{23} & 0 \\ 0 & 0 & 0 & 0 & 0 & G_{13} \end{pmatrix} \quad (10)$$

$$\tilde{C}_n = \underline{\underline{M}}_n : \underline{\underline{C}}_e : \underline{\underline{M}}_n \quad (11)$$

The trial yield function was calculated using Eq. (12):

$$f_{n+1}^{trial} = f_{n+1}^{p*}(\underline{g}_{n+1}^{Trial}, X_n, R_n, \underline{d}_n) = \|\tilde{Z}_{n+1}^{Trial}\| - \tilde{R}_n - \sigma_y \quad (12)$$

$$\|\tilde{Z}_{n+1}^{Trial}\| = \sqrt{\tilde{Z}_{n+1}^{Trial} \cdot \underline{H} : \tilde{Z}_{n+1}^{Trial}} \quad (13)$$

$$\begin{pmatrix} G+H & -H & -G & 0 & 0 & 0 \\ -H & F+H & -F & 0 & 0 & 0 \\ -G & -F & F+G & 0 & 0 & 0 \\ 0 & 0 & 0 & 2N & 0 & 0 \\ 0 & 0 & 0 & 0 & 2L & 0 \\ 0 & 0 & 0 & 0 & 0 & 2M \end{pmatrix} \quad (14)$$

$$\tilde{Z}_{n+1}^{Trial} = \underline{M}_n^{-1} : \underline{Z}_{n+1}^{TrialD} \quad (15)$$

$$\underline{Z}_{n+1}^{TrialD} = \tilde{\underline{g}}_{n+1}^{trialD} - X_n \quad (16)$$

$$X_n = \rho \frac{\partial \varphi}{\partial \alpha} = \underline{C}_n : \alpha \quad (17)$$

$$\underline{C}_n = \underline{M}_n^T : \underline{C} : \underline{M}_n = \frac{2}{3} C \underline{M}^D : \underline{M}^D, \underline{C} = \frac{2}{3} C \underline{I} \quad (18)$$

$$\tilde{R}_n = \frac{R_n}{\sqrt{1 - \|\underline{d}_n\|}} \quad (19)$$

$$R_n = \rho \frac{\partial \varphi}{\partial r} = \tilde{Q} r_n, \tilde{Q} = Q(1 - \|\underline{d}_n\|) \quad (20)$$

At this stage, the plastic admissibility is checked. If $f < 0$, then the elastic assumption is valid and the variables are updated. If $f > 0$, then the elastic assumption is not valid and plastic deformation has occurred. The condition of plastic compatibility is applied and it is necessary that the return occurs on the yield surface.

2- Plastic corrector (Return mapping):

The set of nonlinear equations is according to Eqs. (21) to (23):

$$f_{n+1}^p(\Delta\lambda, \tilde{\underline{n}}_{n+1}, \underline{d}_{n+1}) = \|\tilde{Z}_{n+1}\| - \frac{R_{n+1}}{\sqrt{1 - \|\underline{d}_{n+1}\|}} - \sigma_y = 0 \quad (21)$$

$$g_{n+1}^n(\Delta\lambda, \tilde{\underline{n}}_{n+1}, \underline{d}_{n+1}) = \underline{H} : \tilde{Z}_{n+1} - \|\tilde{Z}_{n+1}\| \tilde{\underline{n}}_{n+1} = 0 \quad (22)$$

$$g_{n+1}^d(\Delta\lambda, \tilde{\underline{n}}_{n+1}, \underline{d}_{n+1}) = \underline{d}_{n+1} - \underline{d}_n - \frac{\Delta\lambda}{(1 - \|\underline{d}_{n+1}\|)^\beta} \left(\frac{\|\underline{Y}_{n+1}\| - Y_0}{S} \right)^s \tilde{\underline{n}}_{n+1} : \underline{M}_{n+1}^{-1} = 0 \quad (23)$$

Finally, the set of nonlinear equations was reduced to two equations with two unknowns (the number of six unknowns for $\tilde{\underline{n}}_{n+1}$ and one unknown for $\Delta\lambda^p$) according to Table 4.

After the convergence of the Newton-Raphson solution, the unknowns were calculated and all the parameters were updated using them. The introduced algorithm was implemented with the help of a Fortran language subroutine and ABAQUS finite element software was used for simulation.

The numerical simulations of the bulk workability tests were performed through a succession of displacement increments for each modeling case. No remeshing operations were performed, and the overall computing time for a typical 3D analysis containing 2500 elements was below 180 min on a standard laptop computer equipped with an Intel i7 CPU processor. For C22000 alloy, density and DEVAR and User material were applied as material properties. The non-linear solution of the process was defined by the explicit solution of the dynamics. All contacts were defined surface to surface using the penalty method. The friction coefficient was determined according to the ring compression test. The meshing for C22000 alloy used 3D stress (C3D8R) linear family element type with Hex element shape, Sweep technique and Medial axis algorithm. FEM results are shown in Table 5. After running the program and analyzing the tests in ABAQUS, different strain paths were drawn on the axial strain and circumferential strain diagrams. Their endpoints were selected as fracture points. All endpoints were fitted and interpolated by fracture line. Fracture line was drawn based on the critical damage level extracted from FEM. The right side of the workability diagram for C22000 alloy for bulk forming processes with critical damage in FEM is shown in Fig. 5.

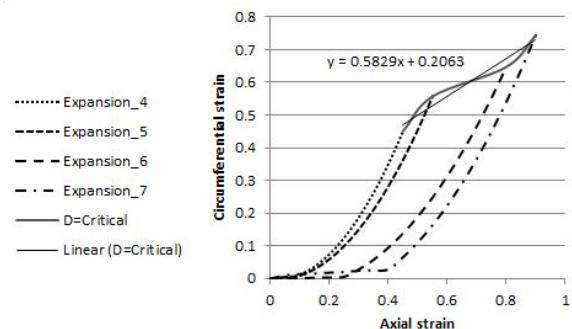


Fig. 5. The right side of workability of C22000 alloy for bulk forming processes in FEM.

Table 4. Newton-Raphson linearization algorithm

Solve the set of nonlinear equations

$$f_{n+1}^p(\Delta\lambda^p, \tilde{n}_{n+1}) = \|\tilde{Z}_{n+1}\|_H - \tilde{R}_{n+1} \cdot \sigma_Y = 0$$

$$g_{n+1}^n(\Delta\lambda, \tilde{n}_{n+1}^p) = \underline{H} : \tilde{Z}_{n+1} \cdot \|\tilde{Z}_{n+1}\| \tilde{n}_{n+1}^p = 0$$

The Newton-Raphson linearization algorithm for solving the above system of equations was presented using the first-order Taylor expansion approximation.

$$R = \left\{ \begin{matrix} f^p \\ g^n \end{matrix} \right\}_{n+1}^{s+1} = \left\{ \begin{matrix} f^p \\ g^n \end{matrix} \right\}_{n+1}^s + \begin{bmatrix} \frac{\partial f^p}{\partial \Delta\lambda^p} & \frac{\partial f^p}{\partial \tilde{n}} \\ \frac{\partial g^n}{\partial \Delta\lambda^p} & \frac{\partial g^n}{\partial \tilde{n}} \end{bmatrix}_{n+1}^s \begin{Bmatrix} \delta\Delta\lambda^p \\ \delta\tilde{n} \end{Bmatrix} + 0 \times \{ \dots \} = \begin{pmatrix} 0 \\ 0 \end{pmatrix}$$

From which the unknowns' corrections, for the iteration (s) under concern, were deduced

$$\begin{Bmatrix} \delta\Delta\lambda^p \\ \delta\tilde{n} \end{Bmatrix} = - \begin{bmatrix} \frac{\partial f^p}{\partial \Delta\lambda^p} & \frac{\partial f^p}{\partial \tilde{n}} \\ \frac{\partial g^n}{\partial \Delta\lambda^p} & \frac{\partial g^n}{\partial \tilde{n}} \end{bmatrix}_{n+1}^s \begin{Bmatrix} f^p \\ g^n \end{Bmatrix}_{n+1}^s$$

In each iteration of the Newton-Raphson solution, the unknowns of the system of nonlinear equations were extracted

$$\delta\Delta\lambda^p = \frac{-(f^p)_{n+1}^s + \left[\frac{\partial f^p}{\partial \tilde{n}} \right]_{n+1}^s : \left[\frac{\partial g^n}{\partial \tilde{n}} \right]_{n+1}^{-1} : g_{n+1}^s}{\left[\frac{\partial f^p}{\partial \Delta\lambda^p} \right]_{n+1}^s - \left[\frac{\partial f^p}{\partial \tilde{n}} \right]_{n+1}^s : \left[\frac{\partial g^n}{\partial \tilde{n}} \right]_{n+1}^{-1} : \left[\frac{\partial g^n}{\partial \Delta\lambda^p} \right]_{n+1}^s}$$

$$\delta\tilde{n} = - \left[\frac{\partial g^n}{\partial \tilde{n}} \right]_{n+1}^{-1} : \left[(g_{n+1}^n)^s + \left[\frac{\partial g^n}{\partial \Delta\lambda^p} \right]_{n+1}^s \delta\Delta\lambda^p \right]$$

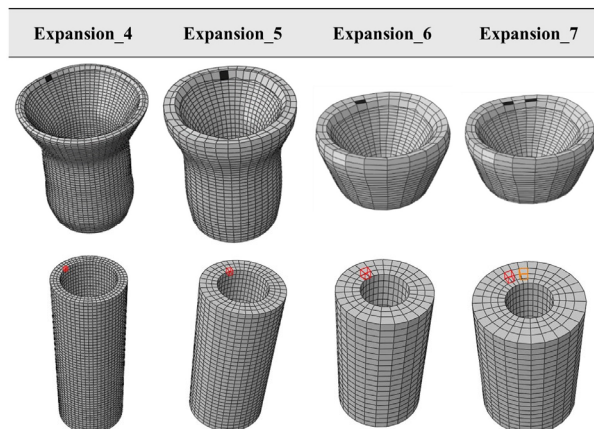
In each iteration Inside the Newton-Raphson solution, the damage tensor levels were calculated using following approximation.

$$d_{n+1} = d_n + \Delta\lambda^p \frac{[M_n^{-1} : \tilde{n}_{n+1}]}{(1 - \|d_n\|)^\beta} \left(\frac{Y_{n+1}((\Delta\lambda^p, \tilde{n}_{n+1}, d_n)) - Y_0}{S} \right)^s$$

It is worth noting that the Eigenvalues of the damage tensor were calculated from damage components given by the above equation, using an appropriate subroutine (Jacobi method) to compute the Eigenvalues and associated Eigenvectors of the damage tensor.

Convergence check?

IF $|R| < Tol$ THEN END Loop

Table 5. Location of the crack in FEM results

5. Results and Discussion

Load-displacement curves for C22000 alloy for all desired geometries in FEM results are shown in Fig. 6. In these curves, it can be seen that all the samples under the given friction conditions take more loads for higher deformation. Fig. 6 also shows the experimental and finite element predicted evolution of the load with displacement for the 'ring expansion' performed with test specimens identified as 'Expansion_7'. Experimental loads show that the geometry of sample also affects the load required for the deformation process.

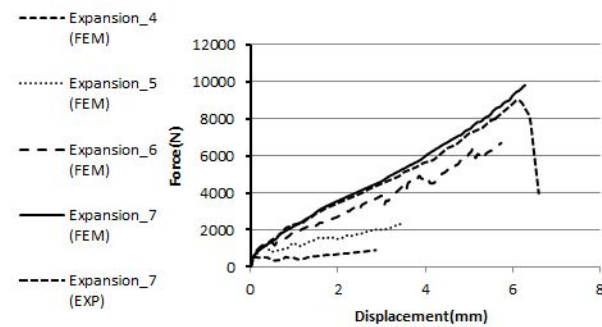


Fig. 6. Experimental and FEM predicted evolution of the load with displacement for ring expansion tests.

The exact moment of cracking is obtained using an experimental test. This test is based on this phenomenon, which is characterized by crack initiation with a drop in force. Comparison of the numerical and experimental result show good agreement.

In previous studies, the Saanouni damage model has not been used to extract the right side of the workability diagram, and the behavior of the C22000 alloy has not been analyzed using the Saanouni damage model. Therefore, in this study, extracting the right side of the workability diagram in bulk metal forming with the help of Saanouni anisotropic damage mechanics criteria is desired. However, the damage level is unknown in this diagram. Thus, with this method, the extraction of the diagram was performed more comprehensively. The only point of fracture was not considered. Different levels of damage and damage evolution can be used to express different regions of the workability diagram. The use of FEM for extracting workability diagrams has helped to determine the damage levels in different strain paths and shows that the damage growth starts from the zero-damage point and ends at the critical damage point. Taking into account the evolutionary process of damage growth from zero to the critical damage value, different fracture lines have been imagined. In Fig. 7, the extracted curves were fitted by the fracture lines and the C22000 alloy workability diagram was extracted for bulk forming processes. The fracture lines with different values of 0.1, 0.2, 0.3 and critical damage were drawn in the FEM results. Different levels of damage and damage evolution can be used to express different regions of the workability diagram.

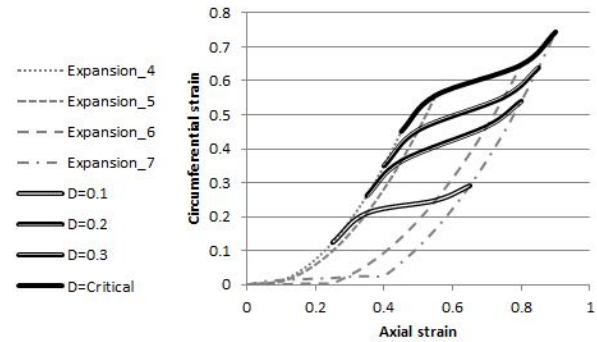


Fig. 7. The right side of workability of C22000 alloy for bulk forming processes with different values of damage.

The purpose of the microstructure analysis is twofolds. First, the location, shape and distribution of voids are visualized within the microstructure. Second, void fractions are measured. After standard metallographic preparation and etching with a solution (10 mL HNO₃ and 90 mL H₂O), cross-sections of the test samples were imaged by SEM (scanning electron microscopic), operating at 30 kV.

The test geometry shown in Fig. 8 provides evidence of cracking in opening mode I, characterized by a fibrous pattern with dimples, due to circumferential tensile stresses acting in the wall thickness.

According to Fig. 8(a), in thin-walled discs (such as Expansion_4 and Expansion_5), cracks are initiated near the bore and propagated first to the bore, then outward to the rim along an inclined shear path. In contrast, according Fig. 8(b), in thick-walled discs (such as Expansion_6 and Expansion_7), cracks are initiated on the upper and lower surface at locations between the inner and outer diameters.

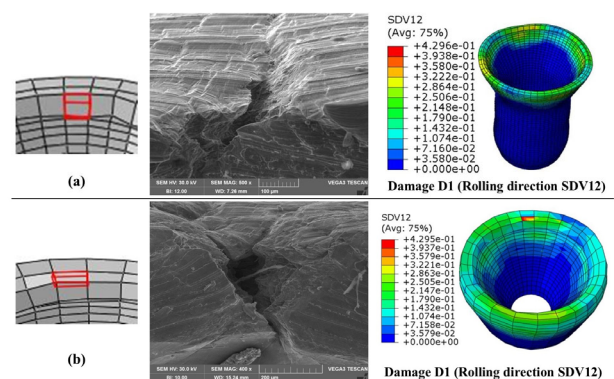


Fig. 8. Experimental fracture strain for geometry: (a) Expansion_4 and (b) Expansion_7 with an image of the crack in the wall thickness compared to Damage D1.

Ductile fracture, governed by void growth and coalescence, strongly depended on stress triaxiality. In terms of micromechanics, the final fracture phase is achieved by the link-void formation. Fracture in metal forming can occur in three different modes: (i) tensile; (ii) in-plane shear; and (iii) out-of-plane shear (which correspond to modes I, II and III of fracture mechanics). The circumstances under which each mode occurs are identified in terms of plastic flow and microstructural ductile damage. Experimental results retrieved from the literature support the presentation and show that plastic flow and fracture in sheet forming result from the competition between modes I and II, where in bulk forming, fracture results from the competition between modes I and III [22].

The ductile fracture mechanism of mode (I) loading is well known. This mechanism is induced by the high hydrostatic stress state and causes a dimple rupture. It is clear that the critical point of the damage is in these elements. These elements first reach the critical damage value and fail. To verify this conclusion, SEM was used to observe the surface of fracture. In Fig. 9 the microstructure of the fracture surface is shown. The profile of the simulation also fits well with the real fracture surface, and from the pictures, many typical void-dimple structures are visible on the surface, which indicates tensional failure (mode I).

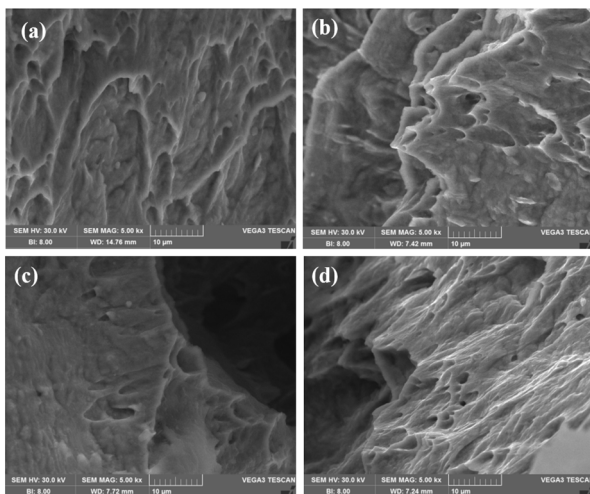


Fig. 9. SEM fractograph showing a dimple fracture surface of C22000; (a) Expansion_4, (b) Expansion_5, (c) Expansion_6, and (d) Expansion_7.

Experimental works available in the literature, have evidenced two regimes of ductile fracture of metals and alloys: a high hydrostatic tension regime, in which fracture results from micro-void nucleation, growth and coalescence, and a shear-pressure-dominated regime, in which fracture is controlled by shear strain localization [23].

In ring expansion, the fracture mechanism is described by cavity nucleation/growth and coalescence mechanism, typical of positive triaxiality. With FEM, accumulated damage value (the sum of damage increments irrespective of sign and direction) at the onset of fracture was estimated for ring expansion with a stepped conical punch. According to Fig. 10, the largest value of accumulated damage and positive triaxiality were occurred at the onset of fracture. It is well known that a higher level of stress triaxiality promotes earlier fracture.

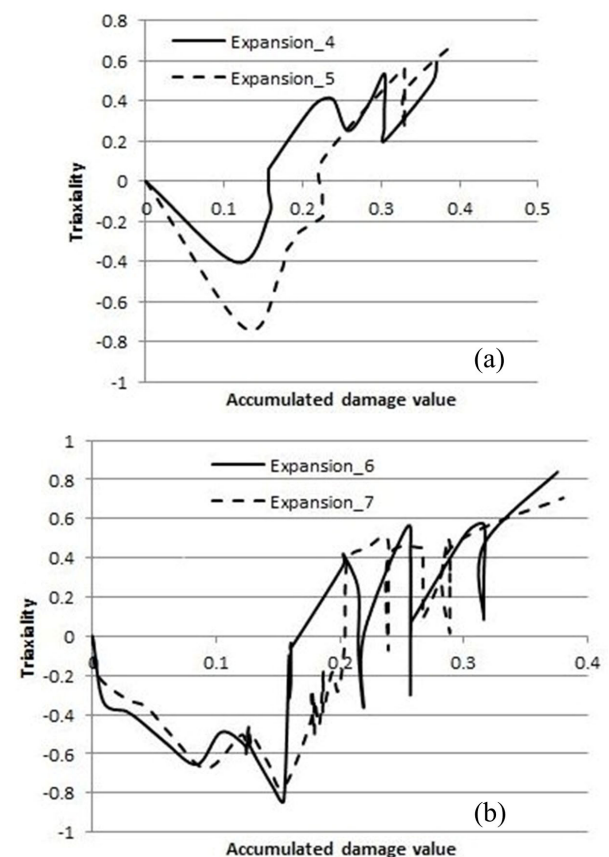


Fig. 10. Accumulated damage and positive triaxiality occurs at the onset of fracture: (a) in Expansion_4 and Expansion_5, (b) in Expansion_6 and Expansion_7.

6. Conclusion

The used ring expansion test performed with a stepped conical punch was proven adequate to replicate three-dimensional stress loading under a wide range of stress triaxiality by varying the wall thickness of the specimens.

By conducting tests, the right side of workability diagram for C22000 alloy was determined. The workability limit approved to be a useful tool in the design and manufacturing stages of any product for bulk forming processes. Successful prediction of workability was feasible only through the method of continuous damage mechanics. Thermodynamically consistent, non-associative and fully anisotropic elastoplastic constitutive equations strongly coupled with ductile anisotropic damage developed in previous work were used to study ring expansion tests, which includes Hill's yield criterion and combined nonlinear isotropic and kinematic hardening. The implemented formulation was defined in the framework of thermodynamics of irreversible processes and a symmetric second-order tensor was adopted to describe the anisotropic damage state variable. The damage model is implemented with VUMAT coding and ABAQUS/Explicit software, and it is used to simulate tests.

The use of FEM solutions for extracting workability diagrams helped determine the damage levels in different strain paths and showed that the damage growth starts from the zero-damage point and ends at the critical damage point. Taking into account the evolutionary process of damage growth from zero to the critical damage value, different fracture lines have imagined.

This study on the characterization of fracture in C22000 alloy made use of ring expansion with a stepped conical punch to determine the strains and the critical ductile damage at the onset of fracture by cracking in opening mode I (tension). An extensive scanning electron microscopic (SEM) study was undertaken to access the underlying ductile fracture mechanisms in these materials at different stress triaxiality levels. Stress triaxiality is one of the parameters that has a significant effect on crack initiation. The measured ductility at fracture decreases as triaxiality increases. High

triaxiality makes materials brittle. Therefore, the brittleness and ductility behavior of materials depends on the type of loading in addition to the type of material.

Acknowledgements

This work was supported by Faculty of Material and Manufacturing Technologies of Malek Ashtar University of Technology in Iran.

Conflict of interest

The authors declare that they have no conflict of interest.

Funding

There is no funding available.

7. References

- [1] Wifi, A. S., Abdel-Hamid, A. & El-Abbasi, N. (1998). Computer-aided evaluation of workability in bulk forming processes. *Journal of Materials Processing Technology*, 77(1-3), 285-293. [https://doi.org/10.1016/s0924-0136\(97\)00430-5](https://doi.org/10.1016/s0924-0136(97)00430-5)
- [2] Tie-Jun, W. (1992). Unified CDM model and local criterion for ductile fracture - II. ductile fracture local criterion based on the CDM model. *Engineering Fracture Mechanics*, 42(1), 185-193. [https://doi.org/10.1016/0013-7944\(92\)90290-U](https://doi.org/10.1016/0013-7944(92)90290-U)
- [3] Lemaitre, J. (1985). A continuum damage mechanics model for ductile fracture. *Journal of Engineering Materials and Technology*, 107(1), 83-89. <https://doi.org/10.1115/1.3225775>
- [4] Kuhn, H. A. (1978). Formability topics-metallic materials. *ASTM STP*, 647, 206-219.
- [5] Semiatin, S. L. (1996). *Forming and forging* (Vol. 14). ASM international.
- [6] Salehi Nasab, A., & Mashayekhi, M. (2019). Application of an efficient anisotropic damage model to the prediction of the failure of metal forming processes. *International Journal of Damage Mechanics*, 28(10), 1-24. <https://doi.org/10.1177/1056789519833726>
- [7] Yetna N'Jock, M., Badreddine, H., Labergere, C., Yue, Z., Saanouni, K., & Dang, V. T. (2021). An application of fully coupled ductile damage model considering induced anisotropies on springback prediction of advanced high strength steel materials. *International Journal of Material Forming*, 14(4), 739-752. <https://doi.org/10.1007/s12289-020-01582-9>
- [8] Yue, Z. M., Badreddine, H., Dang, T., Saanouni, K., & Tekkaya, A. E. (2015). Formability prediction of Al7020 with experimental and numerical failure criteria. *Journal*

- of *Materials Processing Technology*, 218, 80–88.
<https://doi.org/10.1016/j.jmatprotec.2014.11.034>
- [9] Msolli, S., Badreddine, H., Labergere, C., Martiny, M., Robin, G., Jrad, M., Saanouni, K., & Choquart, F. (2015). Experimental characterization and numerical prediction of ductile damage in forming of AA1050-O sheets. *International Journal of Mechanical Sciences*, 99, 262–273. <https://doi.org/10.1016/j.ijmecsci.2015.05.020>
- [10] Saanouni, K. (2008). On the numerical prediction of the ductile fracture in metal forming. *Engineering Fracture Mechanics*, 75(11), 3545–3559.
<https://doi.org/10.1016/j.engfracmech.2007.02.023>
- [11] Saanouni, K., & Lestriez, P. (2009). Modelling and numerical simulation of ductile damage in bulk metal forming. *Steel Research International*, 80(9), 645–657.
<https://doi.org/10.2374/SRI08SP166>
- [12] Rajhi, W., Saanouni, K., & H. Sidhom, H. (2014). Anisotropic ductile damage fully coupled with anisotropic plastic flow: modeling, experimental validation, and application to metal forming simulation. *International Journal of Damage Mechanics*, 23(8), 1211–1256. <https://doi.org/10.1177/1056789514524076>
- [13] Hosford, W. F. & Caddell, R. M. (2011). *Metal forming mechanics and metallurgy*. Cambridge university press.
- [14] Silva, C. M. A., Alves, L. M., Nielsen, C. V., Atkins, A. G., & Martins, P. A. F. (2015). Failure by fracture in bulk metal forming. *Journal of Materials Processing Technology*, 215, 287–298.
<https://doi.org/10.1016/j.jmatprotec.2014.08.023>
- [15] Male, A. T., & Cockcroft, M. G. (1966). A method for the determination of the coefficient of friction of metals under conditions of bulk plastic deformation. *Wear*, 9(3), 38. [https://doi.org/10.1016/0043-1648\(66\)90161-X](https://doi.org/10.1016/0043-1648(66)90161-X)
- [16] Saanouni, K. (2012). *Damage mechanics in metal forming: advanced modeling and numerical simulation*. ISTE/Wiley, London.
- [17] Badreddine, H., Saanouni, K., & Nguyen, T. (2015). Damage anisotropy and its effect on the plastic anisotropy evolution under finite strains. *International Journal of Solids and Structures*, 63, 11–31.
<https://doi.org/10.1016/j.ijsolstr.2015.02.009>
- [18] Murakami, S., & Ohno, N. (1981). *A continuum theory of creep and creep damage*. Springer, Berlin.
- [19] Panakkal, J. P. (1991). Use of longitudinal ultrasonic velocity as a predictor of elastic moduli and density of sintered uranium dioxide. *IEEE Transactions on Ultrasonics, Ferroelectrics, and Frequency Control*, 38(3), 161–165. <https://doi.org/10.1109/58.79598>
- [20] Kitamura, K., & Terano, M. (2014). Determination of local properties of plastic anisotropy in thick plate by small-cube compression test for precise simulation of plate forging. *CIRP Annals*, 63(1), 293–296.
<https://doi.org/10.1016/j.cirp.2014.03.038>
- [21] Saanouni, K., & Chaboche, J. L. (2003). Computational damage mechanics. Application to metal forming. Simulation. *Comprehensive Structural Integrity*, 3, 321–376. <https://doi.org/10.1016/B0-08-043749-4/03072-X>
- [22] Martins, P. A. F., Bay, N., Tekkaya, A. E., & Atkins, A. G. (2014). Characterization of fracture loci in metal forming. *International Journal of Mechanical Sciences*, 83, 112–123.
<https://doi.org/10.1016/j.ijmecsci.2014.04.003>
- [23] De Soto, M. R., Doquet, V., Longere, P., & Papisidero, J. (2022). Anisotropic, rate-dependent ductile fracture of Ti-6Al-4V alloy. *International Journal of Damage Mechanics*, 31(3), 374–402.
<https://doi.org/10.1177/10567895211036491>